Journal of
Materials Chemistry C

REVIEW

View Article Online
View Journal | View Issue

Check for updates

Cite this: *J. Mater. Chem. C*, 2018, **6**, 11853

Received 17th June 2018,
Accepted 30th July 2018

DOI: 10.1039/c8tc02977f

rsc.li/materials-c

Three applications of ultrafast transient absorption spectroscopy of semiconductor thin films: spectroelectrochemistry, microscopy, and identification of thermal contributions

Kathryn E. Knowles, * Melissa D. Koch † and Jacob L. Shelton †

This review describes three recent developments in ultrafast transient absorption spectroscopy that have revealed new insights into the dynamics of photogenerated charge carriers in solution-processed semiconductor thin films. Transient absorption spectroelectrochemistry, in which transient absorption spectra are collected on a semiconductor film immersed in electrolyte solution under an applied potential, provides information about the dependence of transport of photogenerated charges on interfacial electronic structure. Ultrafast transient absorption microscopy enables measurement of excited state dynamics with sub-micron spatial resolution, which has been used to investigate the influence of film morphology on local excited state dynamics and image directly charge transport in solution-processed organic and hybrid organic–inorganic lead-halide perovskite semiconducting films. Finally, the recent identification of significant thermal contributions to the transient absorption spectra of organic and metal oxide semiconductor films is discussed, along with its potential implications for future measurements.

1. Introduction

The performance of any light-activated device based on semiconductors, such as a photodetector, photovoltaic, or photocatalytic system, is determined by the behavior of

Kathryn E. Knowles

Kathryn E. Knowles completed her PhD in chemistry at Northwestern University in 2013 as a DOE Office of Science Graduate Research Fellow studying the effects of surface chemistry on the optical and electronic properties of colloidal semiconductor nanocrystals under the guidance of Prof. Emily Weiss. She earned a DOE Energy Efficiency and Renewable Energy Postdoctoral Research Award to support her research as a postdoc with Prof. Daniel Gamelin at the University of Washington where she studied copper-doped colloidal nanocrystals. Kathryn joined the chemistry department at the University of Rochester in 2016. Her current research interests include synthesis, electrochemistry, and photophysics of binary and ternary first-row transition metal oxide nanomaterials.

Melissa D. Koch

Melissa D. Koch obtained her Bachelor of Science degree in Chemistry from the Rochester Institute of Technology in 2016. Currently she is a PhD student under the supervision of Professor Kathryn Knowles in the department of chemistry at the University of Rochester. Her research interests focus on the micro and spectroscopic characterization of photoactive materials that have a small environmental footprint.

Department of Chemistry, University of Rochester, Rochester, NY 14627, USA. E-mail: kknowles@ur.rochester.edu

† These authors made equal contributions to this work.

photogenerated electrons and holes. Absorption of a photon with energy larger than its bandgap by a semiconductor generates an electron in the conduction band and a hole in the valence band. Every light-activated optoelectronic device based on semiconductors requires separation of these two charges before they recombine. Charge separation is critical to harvesting the electron and hole separately to generate current in a photovoltaic device, reduce or oxidize substrates in a photocatalytic system, or generate a readable voltage in a detector. Processes that limit the performance of these devices typically involve trapping of either the electron or hole to mid-gap states localized at internal defects or at interfaces. Furthermore, the most cost-efficient methods for fabrication of semiconductor devices rely on solution-processing techniques that form semiconductor films with thicknesses on the order of hundreds of nanometers. Compared to single-crystalline semiconductor samples, these solution-processed films have much more heterogeneous structures, with crystalline grain sizes on the order of 100 nm–100 μm, and possibly nano- or mesoporous morphologies with very high surface areas. Consequently, the mechanisms and dynamics of carrier transport in solution-processed semiconductor films tend to be considerably more complex and difficult to parse than those in single-crystalline samples. In order to optimize the design and performance of optoelectronic devices based on solution-processed semiconductors, a thorough understanding of the behavior of photogenerated charge carriers in polycrystalline semiconductor thin films must be established.

Ultrafast pump–probe spectroscopy is a versatile tool that can capture the dynamics of photogenerated carriers as early as hundreds of femtoseconds after photoexcitation. These measurements involve excitation of the semiconductor with a pump pulse at a frequency near or greater than the bandgap followed by a probe pulse at a particular time delay. The transmission of the probe through the sample is measured at various delays both with and without the pump pulse to generate a transient absorption spectrum. Transient absorption spectra are reported in one of two conventions: as a differential transmission or differential absorption spectrum. Both conventions are represented in the data described in this review, and, to minimize confusion, we review them both briefly here. For a differential transmission spectrum, the transmission (defined as the ratio of the transmitted to incident light intensity) measured without the pump pulse is subtracted from the transmission measured with the pump pulse. Data reported in this convention are typically normalized to the linear transmission spectrum measured in the absence of a pump, *i.e.* as $\Delta T/T$. In this convention, positive features correspond to photoinduced transmission due to decreased population of the ground state (ground-state bleach) or stimulated emission, and negative features correspond to photoinduced absorption due to the increased population of photoexcited states. Similarly, a differential absorption spectrum also involves subtracting the absorption spectrum collected without the pump pulse from the absorption spectrum collected with the pump pulse. Eqn (1A) defines absorption, A, in terms of transmission, T, where I represents the transmitted intensity and I_0 represents the incident intensity. The definition of A in eqn (1A) is synonymous with optical density (OD), and ΔA is often reported as ''milli-OD'' (mOD), where the quantity defined by eqn (1A) has been multiplied by a factor of 1000. Eqn (1B) relating ΔA to $\Delta T/T$ follows from eqn (1A). Importantly, we note that ΔA and $\Delta T/T$ have opposite signs. In other words, a positive $\Delta T/T$ signal indicating photoinduced transmission corresponds to a negative ΔA signal and *vice versa.*

$$A = -\log(T) = -\log\left(\frac{I}{I_0}\right) \tag{1A}$$

$$\Delta A = -\log\left(\frac{\Delta T}{T} + 1\right) \tag{1B}$$

The information content of a transient absorption spectrum depends primarily on the frequency of the probe light. Fig. 1 illustrates the transitions and processes accessed at various probe frequencies. Probing in the X-ray or extreme-UV portion of the spectrum provides information about how the electronic structure of individual lattice ions changes upon photoexcitation by examining transitions between core and valence electronic states.[1–3] For example, Hayes *et al.* used an X-ray probe to perform transient absorption measurements at the oxygen and iron K-edges to confirm assignment of transitions observed in the visible absorption spectrum of a hematite (α-Fe_2O_3) film to ligand-to-metal charge transfer (LMCT) transitions.[4] Biswas *et al.* used an extreme-UV probe to examine localization of photoexcited electrons to metal 3d and holes to oxygen 2p states by measuring transient absorption spectra at the oxygen L_1-edge and $M_{2,3}$-edge, respectively.[5] Probing in the UV, visible, or near-infrared parts of the spectrum can provide access to (i) bandgap transitions that excite an electron from the valence band to the conduction band, (ii) sub-bandgap transitions between localized mid-gap trap states and the conduction or valence band, and (iii) intraband transitions of excited electrons in the conduction band or holes in the valence band. The amplitudes of these features can be used to track the populations of excitons or free electrons and holes. Finally, probe frequencies in the terahertz and microwave regimes provide complementary

Jacob L. Shelton

Jacob L. Shelton graduated with a Bachelor of Science in chemistry from Radford University in 2013. He is currently a graduate student in the Knowles lab at the University of Rochester. His research interests include ultrafast transient absorption studies of nanostructured metal oxide semiconductor thin films.

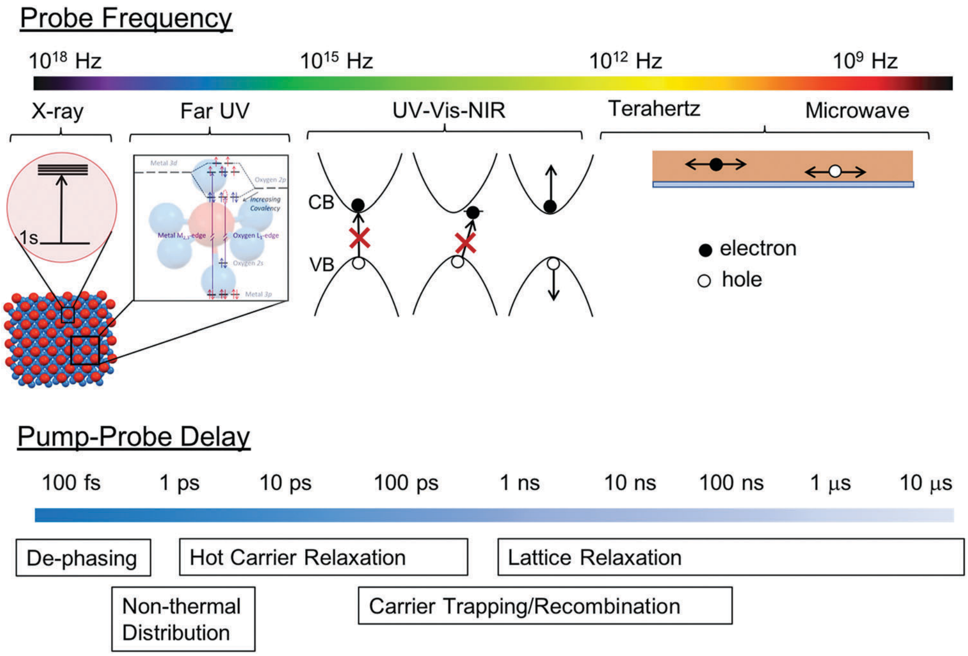

Fig. 1 Illustration of the transitions probed at various frequencies (top) and the processes that occur at various pump–probe delay times (bottom). The red X's in the top indicate transitions that are typically observed as photoinduced transmission (*i.e.*, ground-state bleach) features. The orbital energy diagram depicting transitions probed in the far UV is adapted with permission from ref. 5. Copyright 2018 American Chemical Society.

information about free carrier densities and mobilities on the picosecond–nanosecond and nanosecond–millisecond timescales, respectively.[6,7] All of these probe frequencies have been applied, along with UV or visible pump pulses to excite the bandgap, to thin film semiconductors. This review focuses on transient absorption experiments involving bandgap or above bandgap excitation and UV, visible, and/or near-infrared probes. These probe frequencies are the most accessible experimentally, and thus used most often in pump–probe measurements.

Changing the time delay between the pump and probe pulses enables transient absorption measurements to track the temporal evolution of photoexcited states. Decades of work in this area has revealed a general scheme of processes that occur in semiconductors on various timescales (Fig. 1).[8,9] These processes have historically been divided into four overlapping regimes.[9] First, immediately after photoexcitation exists the coherent regime in which the photogenerated carriers retain the coherent polarization imparted by the laser photoexcitation. Carrier–carrier scattering processes cause these coherences to dephase within hundreds of femtoseconds. Immediately after dephasing, the energy distributions of electrons, holes and excitons are typically non-thermal. Further scattering processes cause these distributions to thermalize within a couple of picoseconds after photoexcitation. Upon thermalization, the temperature of the carriers (electrons, holes, excitons) is usually higher than the lattice temperature, which defines the hot-carrier regime. The primary mechanism by which carriers equilibrate with the lattice is phonon emission.[8,9] Although these hot carrier relaxation processes establish equilibrium between carriers and the lattice within a timescale of 1–100 picoseconds, the semiconductor does not return to thermal equilibrium (*i.e.* its ground state) until all of the photogenerated carriers recombine and the lattice has cooled to ambient temperature. Carrier recombination can occur directly *via* a radiative or nonradiative process involving a conduction band electron and a valence band hole. Alternatively, recombination may involve an electron or hole trapped by mid-gap states located at isolated lattice defects, grain boundaries, or the surface of the semiconductor film. Carrier trapping and recombination typically occur on timescales ranging from one hundred picoseconds to tens of nanoseconds. Few studies have examined lattice relaxation directly, but recent reports of transient absorption measurements of thin-film metal oxide semiconductors (reviewed in detail in the last section of this review) indicate that the timescale of lattice relaxation in these systems is on the order of nanoseconds to tens of microseconds.[4,10]

Many early ultrafast pump–probe measurements of semiconductors examined single crystal or well-defined quantum well samples of direct gap semiconductors and focused on the first two or three temporal regimes.[8,9] For this review, we focus on thin film semiconductor samples fabricated by solution-processing techniques and on measurements examining the dynamics of hot carrier relaxation and carrier trapping/recombination. Due to the large internal and external interfacial areas in solution-processed semiconductor films, carrier trapping processes play a central role in carrier transport in these materials, and these trapping dynamics are strongly influenced by the structure and morphology of the film. Here we provide an overview of three recent developments in the field of transient absorption spectroscopy of semiconductor thin films that focus on elucidating the role of defect states in charge separation and carrier transport, and the influence of film morphology on defect structure and carrier-trapping dynamics. These developments are (i) transient absorption spectroelectrochemistry measurements in which an applied bias is used to investigate mechanisms of interfacial charge transfer in multi-layer devices, (ii) ultrafast transient absorption microscopy (TAM) of semiconductor thin films to examine in detail how the spatial morphology of thin film semiconductors impacts the behavior of photogenerated charge carriers, and (iii) recent identification of thermal contributions to transient absorption spectra of metal oxide thin film semiconductors, which impacts the interpretation of transient absorption spectra collected for these materials. We highlight how these experiments have advanced our understanding of the photophysics and photochemistry of inorganic metal oxide semiconductors, organic semiconductors, and lead halide perovskite films.

2. Transient absorption spectroelectrochemistry

Many optoelectronic devices based on semiconductor thin films rely on internal electric fields generated at interfacial depletion (or "space-charge") regions to promote photoinduced charge separation. For doped semiconductors, these depletion regions form spontaneously at interfaces between the semiconductor and a material with a more positive (in the case of n-type semiconductors) or negative (in the case of p-type semiconductors) Fermi potential. Examples of such interfaces include a p–n heterojunction between two doped semiconductors, which is a key feature of a conventional photovoltaic cell,[11] and a semiconductor–liquid electrolyte junction, which is critical to the operation of a photoelectrochemical cell.[12–14]

Applying a bias to a semiconductor film in an electrochemical cell can induce the formation of a depletion region in an undoped semiconductor or modify the width of a depletion region in a doped semiconductor. Transient absorption measurements as a function of applied electrochemical potential therefore reveal quantitative information about the dependence of the dynamics of photogenerated carriers on the width of the depletion region, which is directly related to the magnitude of the corresponding electric field. When combined with other electrochemical characterization techniques, these transient absorption spectroelectrochemistry measurements enable the identification of specific interfacial or bulk recombination and trapping mechanisms that shorten charge-separated lifetimes and impair device performance. For example, transient absorption spectroelectrochemistry has been used to identify the mechanisms and timescales by which holes located at the surfaces of n-type metal oxide photoanodes, such as α-Fe_2O_3,[15–18] TiO_2,[19] and $BiVO_4$,[20,21] decay under operating conditions for photoelectrochemical water oxidation (*i.e.*, in a working photoelectrochemical cell under anodic bias). Here we highlight the key findings reported for transient absorption spectroelectrochemistry of water oxidation photoanodes; these experiments are reviewed in detail elsewhere.[22,23]

For α-Fe_2O_3, TiO_2, and $BiVO_4$, application of a potential more positive than the flat-band potential increases the lifetime of broad excited-state absorption features associated with photogenerated holes on the tens of microsecond to millisecond timescale.[16,17,19,20] At strong anodic bias, where increased depletion facilitates photocurrent associated with water oxidation, two distinct components emerge in the decay kinetics. The faster (μs–ms) component decays with power law kinetics and is assigned to nongeminate charge recombination between electrons and photogenerated holes that fail to diffuse into the depletion region. The slower (ms–s) component is exponential, with an amplitude and lifetime that both increase with increasing anodic bias. This slower decay is attributed to charge recombination between electrons and holes in the depletion region. Comparison of the potential dependence of the amplitude of the slow decay component assigned to surface-accumulated holes with the potential at which the onset of photocurrent occurs reveals that the transient spectral signatures of holes in the depletion regions of $BiVO_4$ and α-Fe_2O_3 appear at potentials more negative than the photocurrent onset.[17,20] This discrepancy, which can be as high as 600 mV in $BiVO_4$ films,[20] represents the additional bias required to suppress back electron transfer into the depletion region, and may account for the large overpotentials required for water oxidation at $BiVO_4$ and α-Fe_2O_3 photoanodes.

In contrast to the longer timescales, the dependence of ultrafast dynamics of α-Fe_2O_3 and $BiVO_4$ films on applied bias is less consistent. Ultrafast transient absorption measurements of $BiVO_4$ and α-Fe_2O_3 showed no change in the dynamics on the picosecond–nanosecond timescale with increasing anodic bias (Fig. 2E and F).[15,21] However, Si-doped α-Fe_2O_3 films exhibit distinct changes in their ultrafast dynamics under applied bias (Fig. 2A–D).[18] As with the slower timescales, elongation of the lifetime of the photoinduced absorption at λ_{probe} = 750 nm is attributed to suppression of nongeminate charge recombination on the picosecond–nanosecond timescales (Fig. 2A and C). Additionally, the sharper photoinduced absorption at λ_{probe} = 575 nm decays more rapidly with increasing anodic bias and inverts sign at a pump–probe delay of ~100 ps under an applied potential of 1.4 V *versus* the reversible hydrogen electrode (RHE, Fig. 2B and D). This change in sign is attributed to growth of a ground-state bleach feature associated with transitions between the valence band and depleted electron trap states. As the trap states are repopulated with photogenerated electrons on the picosecond timescale, the intensity of absorption into the trap states decreases, which results in growth of a ground-state bleach feature.[18]

In addition to photoelectrochemical systems for water oxidation, transient absorption spectroelectrochemistry has recently been used to study photovoltaic devices, including devices based on lead-halide perovskite films and p-type dye-sensitized solar cells. Perovskite solar cells consist of the photoactive perovskite film sandwiched between electron and hole transport layers.[24] Upon photoexcitation, these layers extract the corresponding carriers from the perovskite and transport them to the external circuit. Efficient charge transfer across the interfaces between the perovskite and carrier transport layers, where charge depletion/accumulation often occurs,[24]

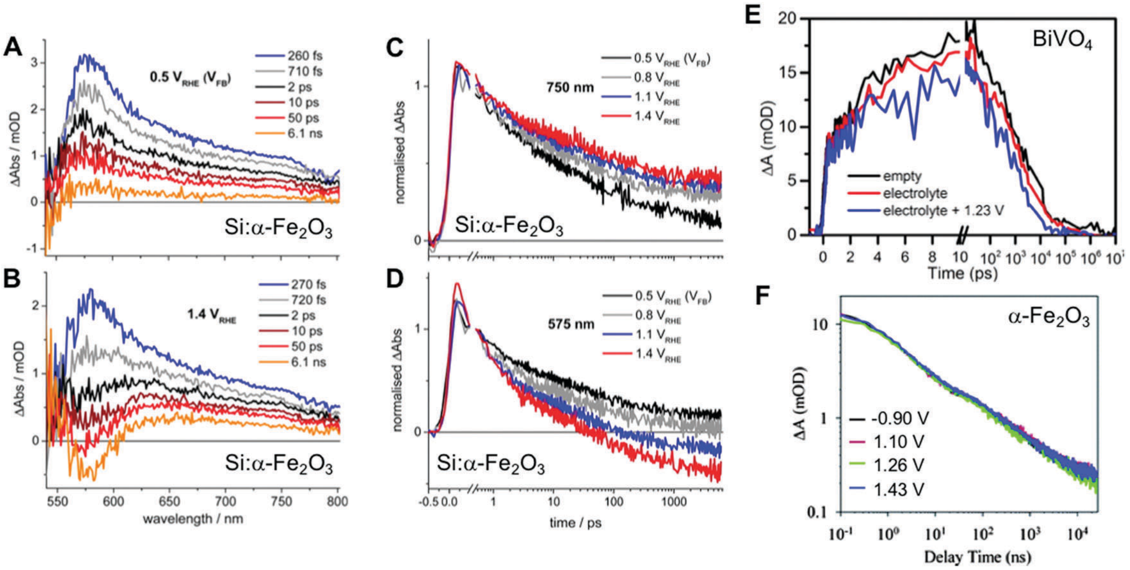

Fig. 2 Ultrafast transient absorption spectroelectrochemistry measurements of metal oxide thin films reported using the differential absorption convention. (A and B) Representative differential absorption spectra of a Si-doped α-Fe_2O_3 film with various pump–probe delays collected at applied potentials of 0.5 V (A) and 1.4 V (B) *versus* RHE with λ_{pump} = 355 nm. (C and D) Corresponding transient absorption kinetics collected for a Si-doped α-Fe_2O_3 film under various applied potentials at λ_{probe} = 750 nm (C) and λ_{probe} = 575 nm (D). The measurements were performed with electrode–electrolyte (*i.e.*, front-side) excitation in a three-electrode cell with the Si-doped α-Fe_2O_3 film as the working electrode, a Pt gauze counter electrode, and a Ag/AgCl reference electrode immersed in a 0.1 M NaOH electrolyte at pH 12.8. Adapted with permission from ref. 18. Copyright 2014 American Chemical Society. (E) Transient absorption kinetics collected at λ_{pump} = 400 nm and λ_{probe} = 475 nm of a $BiVO_4$ film in an empty photoelectrochemical cell (black), in the presence of 0.1 M phosphate buffer at pH 7 (red), and in the presence of electrolyte and an applied bias of 1.23 V relative to a Pt cathode (blue). Adapted with permission from ref. 21. Copyright 2014 American Chemical Society. (F) Transient absorption kinetics collected at λ_{pump} = 400 nm and λ_{probe} = 570 nm of a α-Fe_2O_3 film in a three-electrode cell containing a Pt wire counter electrode and Ag/AgCl reference electrode immersed in 1 M NaOH electrolyte under various applied potentials *versus* RHE. Adapted from ref. 15 with permission from The Royal Society of Chemistry.

is crucial for optimal performance of the photovoltaic device. Transient absorption spectroelectrochemistry would be a useful tool for probing the mechanisms of these interfacial charge transfer processes; however, studying lead halide perovskite films under an applied electrochemical bias is very difficult due to their instability in many commonly used solvents and electrolytes, as well as their sensitivity to even trace amounts of water.[25] Scheidt *et al.* recently overcame these challenges to conduct transient absorption spectroelectrochemical measurements on films of $CsPbBr_3$ nanocrystals spun-cast onto TiO_2 and bare fluorine-doped tin oxide (FTO) substrates.[26] They established that $CsPbBr_3$ is relatively stable within the potential window of −0.6 V to +0.6 V *versus* Ag/AgCl in an electrolyte solution comprising 0.1 M tetrabutylammonium hexafluorophosphate (Bu_4NPF_6) in dichloromethane.[25,26] Scanning to negative potentials beyond this window causes the formation of Pb metal and $CsPF_6$ on the film surface,[25] and scanning to more positive potentials results in oxidation of the Br^- ions.[26] Fig. 3A plots the dynamics of the recovery of the ground-state bleach at λ_{probe} = 520 nm of the FTO/TiO_2/$CsPbBr_3$ film under applied biases ranging from −0.6 to +0.6 V *versus* Ag/AgCl.[26] The rate of recovery increases with increasing anodic bias (Fig. 3B), whereas films of $CsPbBr_3$ on bare FTO (*i.e.* without TiO_2) exhibited no change in bleach recovery kinetics with applied bias (Fig. 3C). These observations indicate that electron depletion of the TiO_2 layer decreases the lifetime of photogenerated electrons in FTO/TiO_2/$CsPbBr_3$ films due to an enhanced rate of electron injection from $CsPbBr_3$ into TiO_2.[26]

Transient absorption spectroelectrochemistry has also recently provided better understanding of charge carrier dynamics in p-type dye-sensitized solar cells based on NiO. In these systems, the production of a reduced dye species upon photoexcitation of the dye is indicative of charge separation *via* hole injection into NiO. The inefficient production of a reduced dye species in NiO cells has long been attributed to low hole mobility in NiO,[27,28] which leads to increased interfacial charge recombination between the dye and the NiO. However, a recent transient absorption spectroelectrochemistry study by Dillon *et al.* shows that the inefficient production of a reduced dye species is due to the presence of mid-gap electron trap states at the surface of the NiO film.[29] For this study, NiO was sensitized with $[Ru^{II}(bpy)_2(4,4'\text{-}(PO_3H_2)_2\text{-}bpy)]^{2+}$ (RuP). Fig. 4 shows the population dynamics measured at various applied biases for both the excited state (Fig. 4a) and reduced dye (Fig. 4b) species. Only at an applied bias of −0.4 V *versus* Ag/AgCl does the excited decay mirror the growth of reduced dye. The disconnect between the kinetics of the excited state and reduced species at more anodic biases is attributed to the existence of vacant intragap electron trap states located energetically just above the valence band of NiO. Fig. 4c shows the normalized density of states near the valence band of NiO measured by cyclic voltammetry over the potential range used in this study. The inflection point around 0.2–0.3 V *versus*

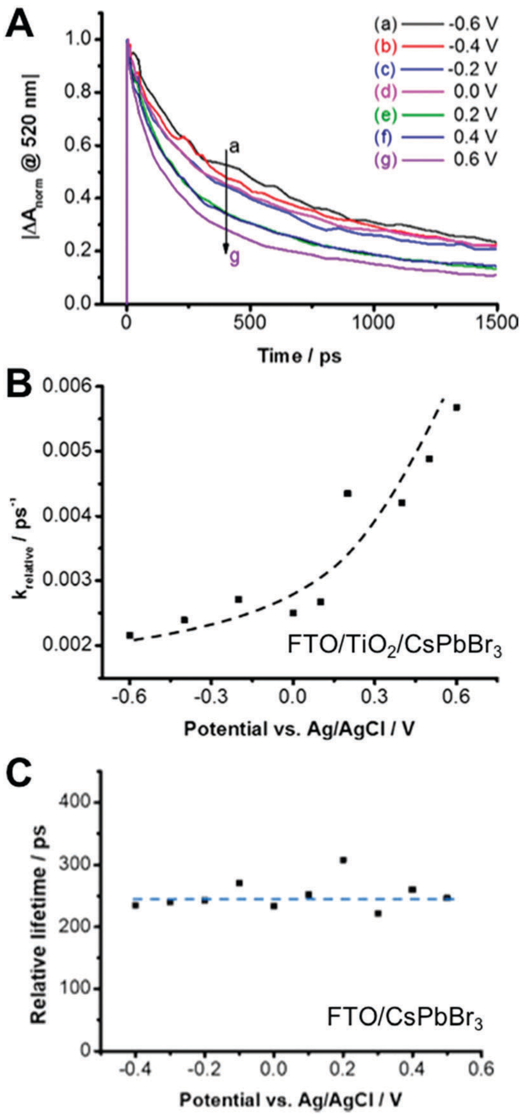

Fig. 3 (A) Kinetics of the recovery of the ground-state bleach of the excitonic band-edge transition of an FTO/TiO_2/$CsPbBr_3$ perovskite film at λ_{probe} = 520 nm collected at applied potentials ranging from −0.6 to +0.6 V *versus* Ag/AgCl. The data are reported as the absolute value of the differential absorption and normalized to the value measured at zero pump–probe delay. (B) Plot of the rate constants for ground-state bleach recovery *versus* applied potential for an FTO/TiO_2/$CsPbBr_3$ film. The dashed line is a guide to the eye. (C) Plot of the lifetime of the ground-state bleach of an FTO/$CsPbBr_3$ film *versus* applied potential. These measurements were carried out in a standard three-electrode setup using the perovskite film as the working electrode, a Pt mesh counter electrode, and an Ag/AgCl reference electrode (calibrated to the ferrocene/ferrocenium redox couple), submerged in deaerated dichloromethane containing 0.1 M Bu_4NPF_6. Adapted with permission from ref. 26. Copyright 2018 American Chemical Society.

Ag/AgCl indicates the transition from intragap states to the valence band, and the long tail into negative potentials indicates the presence of a large distribution of intragap states near the valence band.[29] The application of cathodic bias fills these trap states and enables successful charge separation.[29]

In general, transient absorption spectroelectrochemistry measurements, such as those highlighted here, provide useful insight about photogenerated carrier transport across interfaces in semiconductor thin films. Using transient absorption to measure the response of carrier dynamics to the magnitude of applied bias enables the elucidation of specific mechanisms that promote charge separation. Such measurements contribute to improved rational design of light-activated optoelectronic devices in which carriers must travel across one or more interfaces.

3. Ultrafast transient absorption microscopy

Ultrafast transient absorption microscopy (TAM) provides a means by which to track the evolution of photoexcited states in both time and space. These measurements can be run in three different modalities.[30] (i) Spatially overlapping the pump and probe pulses while scanning their delay time provides information analogous to ensemble transient absorption measurements, but over a much smaller sample region. (ii) Maintaining spatial overlap of the pump and probe pulses while raster scanning the sample at a particular delay time provides a map of the spatial variation in excited state dynamics across the sample, and (iii) fixing the location of the pump pulse and scanning the probe pulse over the sample at various delay times provides information about how a photoexcited state generated at a particular location evolves in space. Temporal resolution of these measurements is on the order of hundreds of femtoseconds and, like conventional pump–probe experiments, is limited by the convoluted width of the pump and probe pulses. Spatial resolution is typically limited by diffraction,[30] but when used to image carrier diffusion (*vide infra*), the spatial resolution is limited by both diffraction and the signal-to-noise ratio of the instrument.[31]

Much of the early implementation of TAM techniques focused on measuring single particles or nanostructures. This work, as well as the more technical details describing how the measurements are actually performed, is reviewed elsewhere.[30,32–35] Here we focus on recent applications of TAM to thin-film semiconductor systems, where it has been used to reveal heterogeneous dynamics of photoexcited states at the internal interfaces of solution-processed organic[36–39] and inorganic[40–45] semiconductor thin films and to image directly carrier transport in lead halide perovskite films.[31,46]

Huang and co-workers used TAM to study solution-processed films comprising blends of poly(3-hexylthiophene) (P3HT, a hole-transporting polymer) and [6,6]-phenyl-C_{61}-butyric acid methyl ester (PCBM, an electron-transporting polymer) fabricated with various compositions and annealing temperatures.[37] Such polymer blend films have potential applications as bulk heterojunction solar cells.[47–49] Thermal annealing of these films tends to produce micron-sized crystals of PCBM where the size and density of the crystals increases with increased PCBM concentration and annealing temperature.[50] Using TAM, Huang and co-workers demonstrated that regions of the film immediately adjacent to a PCBM microcrystal exhibit faster

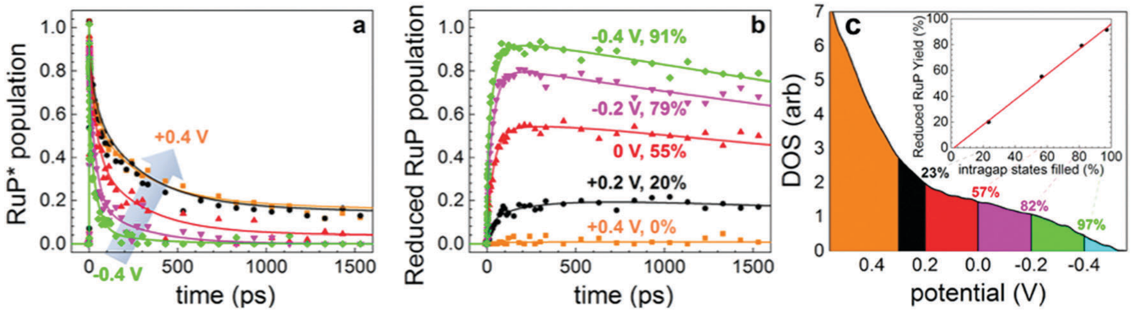

Fig. 4 Population dynamics *versus* applied bias for excited (RuP*, a) and reduced (RuP^-, b) $[Ru^{II}(bpy)_2(4,4'\text{-}(PO_3H_2)_2\text{-}bpy)]^{2+}$ dye bound to a NiO thin film. The dynamics of RuP* were obtained by monitoring the recovery of its ground-state bleach at λ_{probe} = 450 nm, and the dynamics of RuP^- were obtained by monitoring its absorption at λ_{probe} = 520 nm. (c) Normalized density of states (DOS) near the valence band for the NiO films used in this study. The percentages given correspond to the total percent area of intragap states filled in at each potential used in the TA experiments. Inset: Plotting the percent intragap states filled *versus* the maximal yield of RuP^- reveals a linear relationship. All potentials are referenced to Ag/AgCl. Measurements were carried out in a standard three-electrode setup with Pt wire counter electrode and a mini Ag/AgCl reference electrode in 0.1 M acetonitrile solution of Bu_4NPF_6. Adapted with permission from ref. 29. Copyright 2017 American Chemical Society.

excited-state decay than regions farther away from a crystal or overlapping the crystal itself.[37] Correlating the TAM measurements with atomic force microscopy (AFM) enabled the authors to attribute this observation of spatially inhomogeneous excited state dynamics to increased recombination of excitons in P3HT-rich (PCBM-depleted) regions immediately adjacent to a PCBM microcrystal. The slower dynamics observed inside a PCBM crystal were attributed to charge separation between the PCBM crystal and P3HT layers underneath. These observations demonstrate a correlation between the spatial heterogeneity in the dynamics of photogenerated charges and the complex morphology of semiconducting polymer blend films. This correlation confirms that control over the morphology of these films is critical for optimizing their device performance.

Crystalline thin films of organic small-molecule chromophores have also exhibited semiconducting properties of interest for optoelectronic devices.[51] These films tend to exhibit longer-range order than polymer-based films, and their relatively high singlet fission efficiencies make them particularly promising for photovoltaics.[52–54] Singlet fission is a process by which one singlet exciton, produced upon absorption of a single photon, generates two lower-energy triplet excitons. In principle, this process allows a photovoltaic cell to break the Shockley–Quiesser limit by increasing its maximum photocurrent. However, triplet excitons have much slower diffusion constants than singlet excitons,[53] which can make triplet excitons more difficult to harvest in a device. Time-resolved photoluminescence measurements of the lifetime of the singlet state indicate that the morphology of crystalline tetracene films impacts the rate of singlet fission,[54] but luminescence experiments are usually unable to observe the triplet states directly due to their low luminescence quantum yields. Transient absorption measurements are capable of observing both singlet and triplet excited state dynamics directly. Wan *et al.* combined the sensitivity of transient absorption spectroscopy to both singlet and triplet exciton dynamics with the spatial resolution provided by transient absorption microscopy to image directly both singlet and triplet exciton diffusion in single crystals of tetracene.[53] This study revealed a new transport mechanism whereby equilibration between fast-diffusing singlet and slow-diffusing triplet exciton states, mediated by reversible singlet fission, and triplet–triplet annihilation processes, extends the diffusion length of triplet excitons.

The crystalline grain sizes of small-molecule films are usually smaller than the spot sizes of pump and probe pulses used in conventional transient absorption spectroscopy. Therefore, microscopy techniques, such as TAM, are required to distinguish between inter- and intragrain dynamics. An additional advantage of the subdomain spatial resolution provided by TAM is the ability to resolve pump or probe polarization-dependent features due to the fact that all molecules within the excitation volume share the same orientation. Ginsberg and co-workers demonstrated the utility of this approach by applying polarization-resolved TAM measurements to a microcrystalline film of 6,13-bis-(triisopropylsilylethynyl)-pentacene (TIPS-Pn).[39] By fixing the polarization of the pump pulse and rotating the polarization of the probe pulse the authors were able to detect the relative orientations of the transition dipole moments (and, by extension, the molecules) in two adjacent crystalline grains of TIPS-Pn (Fig. 5). Fig. 5c plots the amplitude of the TA signal measured in two adjacent grains *versus* the polarization angle of the probe pulse. Fig. 5d shows the corresponding TAM images. The pump polarization remained constant to ensure that every measurement was conducted with the same excited state population. Both locations exhibit a sinusoidal dependence of TA signal on probe polarization with the same period, but a phase offset of ∼45°. This phase offset indicates that the transition dipole moments associated with transitions at the probe wavelength (λ_{probe} = 700 nm) of these two grains form an angle of ∼45°. Since a transition dipole moment has a fixed orientation relative to the molecular axes, these results indicate that the angle between the molecular orientations of the two grains is also ∼45°. Furthermore, analysis of the probe-polarization dependent dynamics measured in the two grains enabled the authors to assign mechanisms to the various decay components observed.[39] Such analysis would

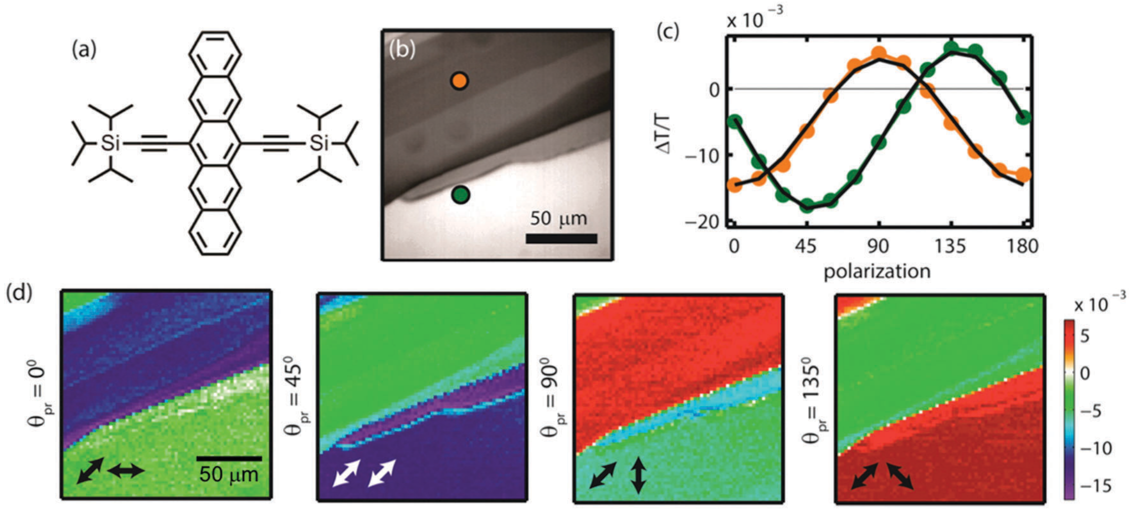

Fig. 5 (a) Structure of TIPS-Pn. (b) Linear transmission image of a TIPS-Pn film illustrating two locations (orange and green) for which TAM measurements were collected. (c) Plot of the differential transmission signal ($\Delta T/T$) *versus* probe polarization angle collected at a pump–probe delay of 100 femtoseconds with a pump polarization of θ_{pump} = 45°. The orange circles plot data collected at the location indicated by the orange spot in (b) and the green circles plot data from the "green" location. (d) Differential transmission images of the region depicted in part (b) collected at a pump–probe delay of 50 femtoseconds with a pump polarization of θ_{pump} = 45° and probe polarizations of θ_{probe} = 0°, 45°, 90°, and 135°. The arrows indicate the polarizations of the pump and probe pulses. Adapted with permission from ref. 39. Copyright 2013 American Chemical Society.

not have been possible with data from a conventional bulk TA measurement.

Lead halide perovskites such as $CsPbX_3$ and $CH_3NH_3PbX_3$, where X = Cl, Br, or I, are perhaps the most exciting and interesting semiconductor materials to emerge over the past decade due to the remarkably high performance achieved in simple solution-processed photovoltaic devices based on these films.[24] Long carrier lifetimes combined with high carrier mobilities are prime candidates to be the origin of the exceptional performance exhibited by perovskite photovoltaics.[7,55,56] However, the dependence of these properties on the exact morphology of a thin film, which can vary significantly from sample to sample when fabricated using solution-based deposition techniques, is not clear. Several groups have recently employed ultrafast transient absorption microscopy to investigate this question.

Guo *et al.* used TAM to image directly the transport of band-edge and hot carriers in solution processed $CH_3NH_3PbI_3$ films (see Fig. 6).[31,46] First, they identified a photoinduced absorption feature spanning 500–700 nm as originating from free carriers in the conduction and/or valence band of the semiconductor.[31] The amplitude of this signal was assumed to be proportional to total carrier density. TAM measurements in which the pump beam was fixed to a particular location on the sample and the probe beam was scanned over the sample at various delay times revealed that the area over which photoinduced absorption amplitude at λ_{probe} = 580 nm was observed increased isotropically with increasing delay time. Fitting this area to a two-dimensional Gaussian function revealed a linear increase of its width (as parameterized by the variance of the Gaussian function) with increasing delay time (see Fig. 6D). The slope of this linear dependence is proportional to the carrier diffusion coefficient. By performing this experiment at different pump locations on the sample, the authors were able to determine that there were only small variations in the value of the carrier diffusion coefficient at different locations in the film. Furthermore, the transport was found to follow diffusive behavior for the entire lifetime of the carriers, which indicated that localized trap states did not have a significant impact on carrier transport.[31]

The same group used a similar technique to map hot carrier transport in a $CH_3NH_3PbI_3$ perovskite film (Fig. 6E). In this case, the probe monitored a sub-bandgap photoinduced absorption feature associated with hot carriers.[46] This feature is thought to arise from a transient electric field generated by energetic hot carriers that induces a bathochromic shift in the band-edge absorption feature due to the Stark effect. The transport of these hot carriers, as measured by tracking the spatial evolution of this feature by scanning the probe beam over the sample while keeping the pump beam at a fixed location, was found to be quasi-ballistic during the lifetime of the hot carrier, then diffusive once the carriers equilibrate with the lattice.[46] This quasi-ballistic transport behavior enables hot carriers in perovskite films to travel ∼600 nm before equilibrating with the lattice. Such long diffusion lengths facilitate harvesting of hot carriers from perovskite photovoltaics, which increases the theoretical maximum power conversion efficiency for a photovoltaic device.

Other transient absorption microscopy studies of near-bandgap spectral features associated with hot carriers in $CH_3NH_3PbI_3$ found significant spatial heterogeneity in these signals. In other words, these signals appear in some film locations, but not others. For example, Simpson *et al.* measured the spatial dependence of transient absorption signal in $CH_3NH_3PbI_3$ films.[41] TAM images were collected by raster scanning the sample while keeping the pump and probe

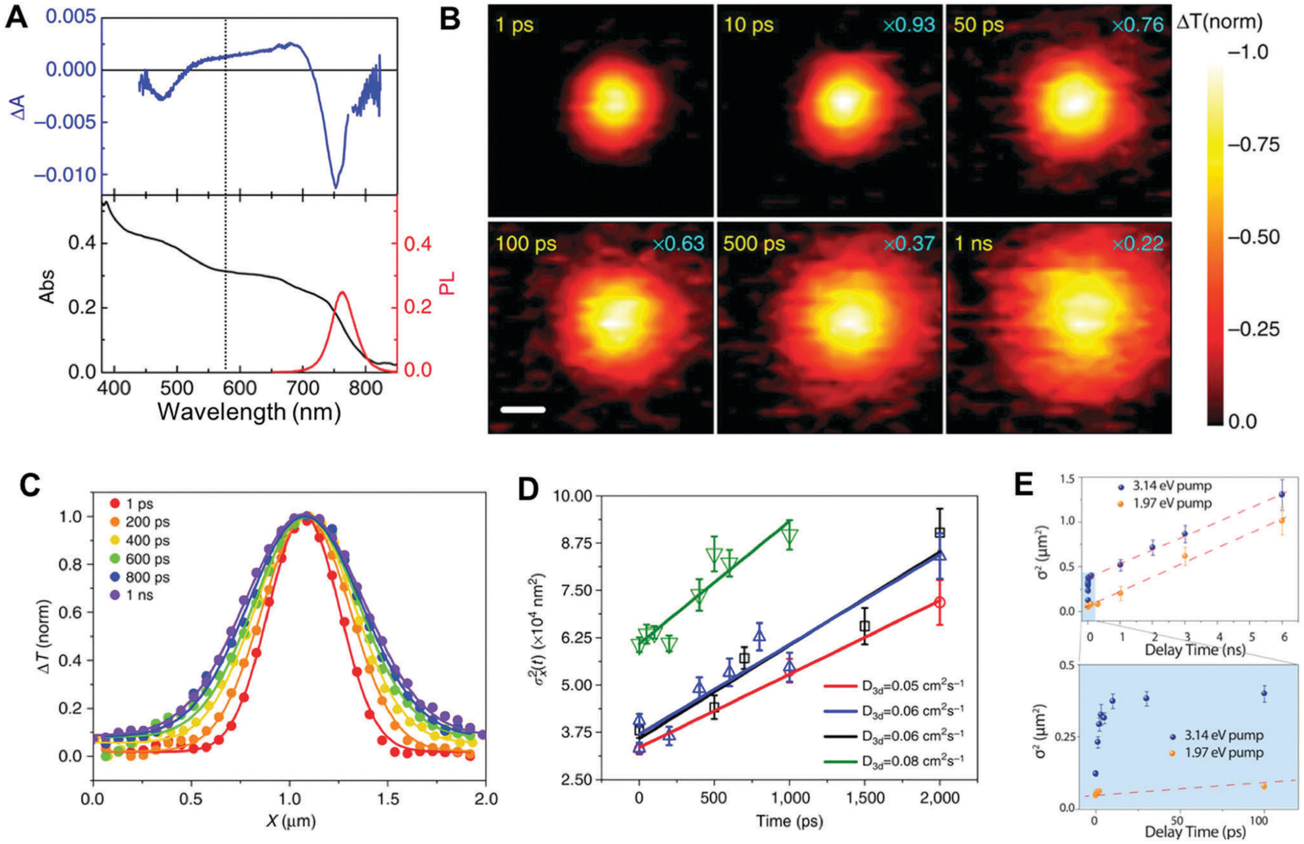

Fig. 6 (A) Top: Differential absorption spectrum of bulk $CH_3NH_3PbI_3$ plotted as ΔA and measured at 50 ps pump–probe delay time. Bottom: Absorption (black) and photoluminescence (red) spectra of a $CH_3NH_3PbI_3$ thin film. The vertical dotted line indicates the probe wavelength used for TAM measurements shown in parts (B–D). (B) Differential transmission ($\Delta T/T$) images of a $CH_3NH_3PbI_3$ film obtained at various delay times (shown in yellow) with a fixed pump location (λ_{pump} = 387 nm) and scanned probe (λ_{probe} = 580 nm). The scale bar is 300 nm. The signal amplitudes for images collected with delay time > 1 ps are normalized to the maximum amplitude measured at 1 ps delay time, and the normalization factors are shown in blue. (C) Profiles of ΔT amplitude (normalized at the peak) obtained from single line scans of the probe beam across the center of one fixed pump location at various time delays. The profiles are fit with Gaussian functions. (D) Plot of the variances of Gaussian profiles from part (C) *versus* pump–probe delay time. Data were collected at four different locations within the same film. The slopes of the linear fits are proportional to the carrier diffusion coefficients, D_{3d}, listed in the bottom right corner of the plot. Adapted with permission from ref. 31. Copyright 2015 Springer Nature. (E) Plot of the variances of Gaussian profiles obtained by scanning a probe beam with λ_{probe} = 787 nm across a pump beam with λ_{pump} = 396 nm (blue) and a pump beam with λ_{pump} = 631 nm (orange) *versus* pump–probe delay time. The bottom panel shows a zoomed-in view of the data plotted in the top panel. Adapted with permission from ref. 46. Copyright 2017 American Association for the Advancement of Science.

spatially overlapped for various pump–probe delays. When pumping at λ_{pump} = 500 nm (well above the bandgap) and probing at λ_{probe} = 800 nm (very close to the bandgap) the authors observed distinct, spatially separated regions of positive and negative signal ($\Delta T/T$) that persisted at all decay times up to ∼150 ps (Fig. 7A). The difference in TA signals between the two regions was attributed to spatially segregated populations of excitons and free carriers.[41] Nah *et al.* observed similar spatial segregation of signals.[44] Spectrally resolving the probe beam by dispersing it onto a CCD detector revealed that regions of net positive or negative spectrally integrated signals were due to transient red or blue shifts of the bandgap, respectively. Red shifts were observed to be present immediately upon photoexcitation, but decayed within ∼1 ps, whereas the blue shifts grew in within 1 ps. The authors attributed the red shift to a hot carrier-induced Stark shift and the blue shift to screening of excitonic transitions by relaxed carriers. The spatial separation of these signals was attributed to local variations in the dielectric of the sample.[44]

Nah *et al.* also recently identified a third signal that appears in some locations of a $CH_3NH_3PbI_3$ film, but not others.[57] This signal is an induced transmission (or ground-state bleach) located at an energy just below the bandgap that starts to grow in approximately one picosecond after photoexcitation. Its energy is slightly different at different locations within the film and its intensity and peak energy both increase with increasing carrier temperature. The authors suggest that this feature has characteristics of both a polaron and an exciton, but additional measurements and theoretical modeling are required to make a definitive assignment. In any case, the feature is completely obscured in ensemble measurements and was only discovered through the use of sub-domain TAM measurements. This result highlights the ability of TAM measurements with high spatial resolution to

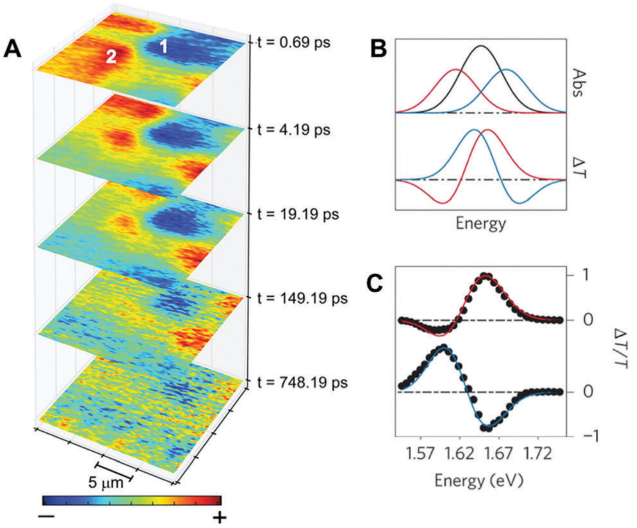

Fig. 7 (A) Spectrally integrated differential transmission images of a $CH_3NH_3PbI_3$ thin film measured at various pump–probe delay times with spatially overlapped pump (λ_{pump} = 500 nm) and probe (λ_{probe} = 800 nm) beams. Spatially separated regions of negative (photo-induced absorption) and positive (photo-induced transmission) signal are labeled 1 and 2, respectively. Adapted with permission from ref. 41. Copyright 2015 American Chemical Society. (B) Illustration of how a shift in the band-edge absorption peak to higher (blue) or lower (red) energies produces a derivative feature in the differential transmission signal. (C) Differential transmission spectra collected from regions in a $CH_3NH_3PbI_3$ thin film that exhibit net positive (red) or net negative (blue) $\Delta T/T$ signal when spectrally integrated. Adapted with permission from ref. 44. Copyright 2017 Springer Nature.

identify and characterize previously undetectable features of heterogeneous semiconductor thin-film materials.

4. Thermal contributions to transient absorption spectra of semiconductor thin films

In some cases, unambiguously assigning spectral features observed in the transient absorption spectrum of a thin-film semiconductor can be quite difficult. In the case of thin films of organic semiconductors, increased temperature produces changes to their absorption spectra that overlap spectral changes associated with electronic excitations.[58–60] Neglecting the effects of thermal energy deposited into a film upon photoexcitation can lead to incorrect assignment of spectral features observed in transient absorption measurements. For example, Rao *et al.* demonstrated that long-lived photoinduced absorption features observed above the bandgap energy in thin films of pentacene and previously attributed to excimers, charged states, or doubly excited excitons are actually due to thermal effects.[59] Two experiments enabled the authors to make this assignment. First, subtracting the absorption spectrum of a pentacene film collected at 280 K from that collected at 300 K produced a thermal difference spectrum with features that matched those observed in the transient absorption spectrum at long delays, with the exception of a broad sub-bandgap photoinduced absorption at λ_{probe} > 720 nm assigned to triplet excited state absorption (Fig. 8A). Thermal difference spectra were also used to account for contributions to transient absorption spectra of thin films of *N*-*N*′-dioctyl-3,4,9,10-perylenedicarboximide from thermal energy released upon relaxation of high-energy singlet states formed upon singlet–singlet annihilation.[60] Second, comparison of transient absorption kinetics measured for pentacene films prepared on silica substrates to those measured for identically prepared films on sapphire substrates revealed faster decay dynamics for the photoinduced absorption feature at λ_{probe} = 620 nm for the films on sapphire compared to silica as shown in Fig. 8B.[59] Sapphire has a higher thermal conductivity than silica and can therefore dissipate thermal energy from the film more efficiently, which leads to faster decays for spectral features associated with thermal energy in the film.[58,59] The ground-state bleach, which also appears in the thermal difference spectrum, also decays slightly faster on a sapphire substrate compared to a silica substrate. Decreasing the temperature decreases the heat capacity of the pentacene film and therefore results in larger thermal effects for the same photoexcitation conditions.[59] Consequently, low temperature transient absorption measurements exhibit a larger difference in decay kinetics between films on sapphire and silica substrates (Fig. 8C). Notably, the decay dynamics of the sub-bandgap photoinduced absorption assigned to triplet excited state absorption are independent of the substrate, consistent with a purely electronic transition. These results illustrate that changing the thermal conductivity of the substrate can help identify which transient absorption features of a thin-film semiconductor have a significant thermal component. This strategy was also used to identify thermal contributions to transient absorption spectra of regioregular poly(3-hexylthiophene) thin films.[58]

Thermal contributions to transient absorption spectra of metal oxide semiconductor thin films have only recently been recognized.[4,10] Here, we consider hematite (α-Fe_2O_3) as an illustrative case study. Hematite thin films have attracted intense interest in recent years due to their performance as visible-light sensitive photoanodes for water oxidation combined with their facile fabrication and inexpensive composition. Transient absorption studies of hematite (α-Fe_2O_3) over the last two decades have illustrated the difficulty in unambiguously assigning transient spectral features to specific excited state transitions. In a study of the ultrafast dynamics of photoexcited colloidal hematite nanoparticles, Cherepy *et al.* found that the observed kinetics were largely independent of both pump power and probe wavelength, with no measureable signal persisting past 100 ps.[61] Furthermore, the dynamics were unchanged by either surface adsorbates (deoxykenocholic acid and orange II) or variations in pH, leading the authors to assign the decay kinetics to non-radiative carrier recombination mediated by intrinsic or internal mid-gap and trap states.[61] Joly *et al.* observed similar dynamics in hematite thin films, but with the addition of a measurable signal lasting hundreds of picoseconds that they attributed to slow relaxation from trap states.[62]

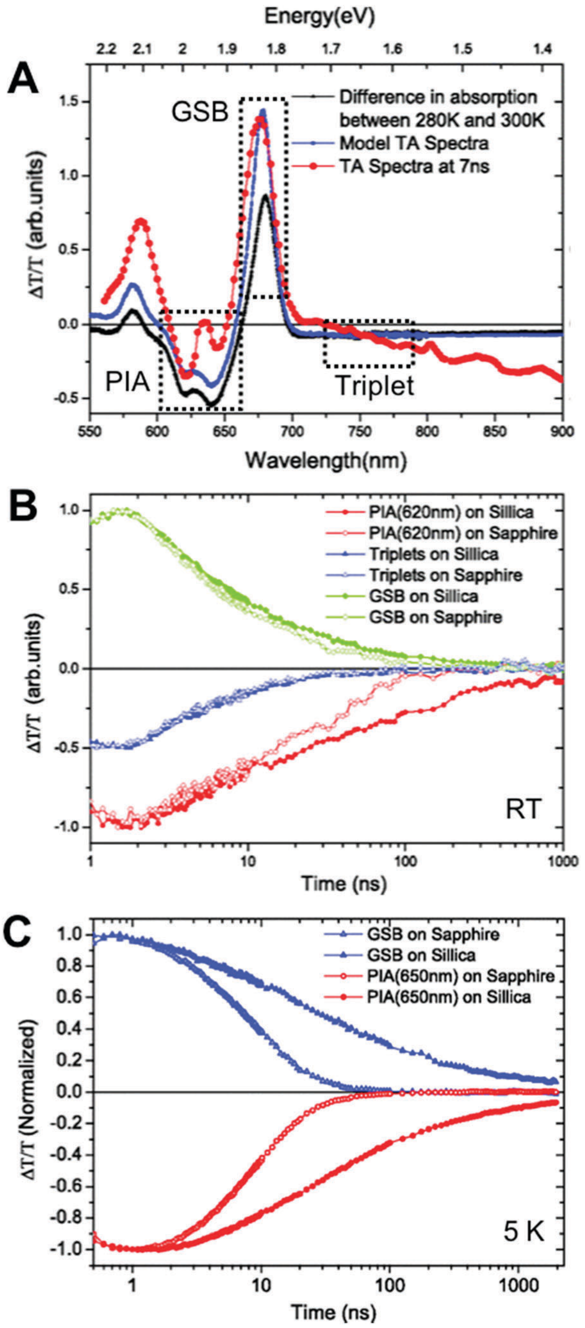

Fig. 8 (A) Thermal difference spectrum (black), predicted transient absorption spectrum including only pump-induced sample heating (blue), and transient absorption spectrum collected with λ_{pump} = 532 nm at a pump–probe delay of 7 ns for a 150 nm thick pentacene film on a silica substrate. All spectra are plotted as differential transmission ($\Delta T/T$). (B) Normalized kinetic traces extracted from transient absorption spectra collected at room temperature for 150 nm thick films of pentacene deposited on silica (closed symbols) or sapphire (open symbols) substrates. The kinetics correspond to the integrated spectral regions indicated by the dashed boxes in part A: ground-state bleach (GSB, λ_{probe} = 660–690 nm, green), photoinduced absorption (PIA, λ_{probe} = 606–626 nm red), and triplet excited state absorption (triplet, λ_{probe} = 720–780 nm, blue). (C) Normalized kinetics extracted from transient absorption spectra collected at 5 K for 150 nm thick films of pentacene deposited on silica (closed symbols) and sapphire (open symbols) substrates. Kinetics from the ground-state bleach (λ_{probe} = 660–680 nm) are shown blue, and kinetics from the photoinduced absorption (λ_{probe} = 630–645 nm) are shown in red. Reprinted with permission from ref. 59. Copyright 2011 by the American Physical Society.

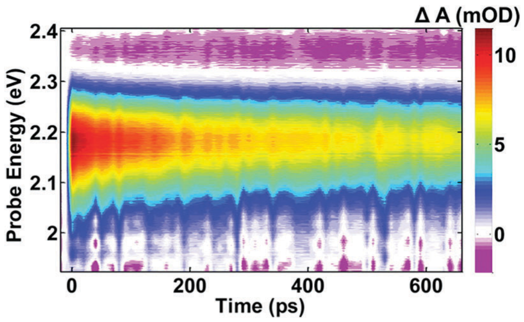

Fig. 9 Transient absorption surface plotted in units of mOD of a hematite thin film pumped at λ_{pump} = 400 nm. Adapted with permission from ref. 63. Copyright 2014 American Chemical Society.

More recently, Sorenson *et al.* performed transient absorption measurements of hematite films extending to 680 ps.[63] The observed spectral evolution is shown in Fig. 9. Based on the sharp, high-energy boundary between positive and negative signal observed at a probe energy of ∼2.3 eV (λ_{probe} = 540 nm), which is indicative of the top of the conduction band, the authors assigned the excited-state absorption features to intraband transitions of free electrons. The long delay features were assigned to continued excited state absorption by electrons that had relaxed to the bottom of the conduction band prior to a slow decay attributed to carrier recombination (>670 ps).[63]

Hayes *et al.* observed similar long-lived signals extending to thousands of picoseconds in their study of hematite thin films; however, they propose that the features persisting beyond 100 ps are due almost entirely to a decrease in the bandgap energy caused by an increase in the lattice temperature arising from hot carrier relaxation *via* phonon emission.[4] The most significant evidence for this attribution is the striking qualitative similarity between the features of the transient absorption spectrum and those of a thermal difference spectrum of the hematite film, both plotted in Fig. 10A. The thermal difference spectrum was obtained by subtracting the steady-state absorbance spectrum of the film collected at 300 K from that collected at 500 K. Representative spectra illustrating the temporal evolution of transient absorption spectra between regions C and E are shown in Fig. 10B and C.[4]

The authors attribute the additional negative signal observed in region C for early delays to ground state bleaching and stimulated emission, while the blue-shift of region D is attributed to the decay of the broad feature in region E (Fig. 10B).[4] This feature, centered at λ_{probe} ∼ 675 nm, is assigned to the absorption of both hot and thermalized carriers in the conduction band, as well as hole-filling transitions from the valence band. The remaining spectral features qualitatively match those of the thermal difference spectrum, suggesting that thermal effects dominate the signal as early as 500 fs after excitation.[4] These signals persist for several microseconds after photoexcitation (Fig. 10C). With increased pump fluence, the authors observed a slight red shift in the region suspected to be dominated by thermal contributions, but no change in the kinetics of this spectral feature. Changing the pump

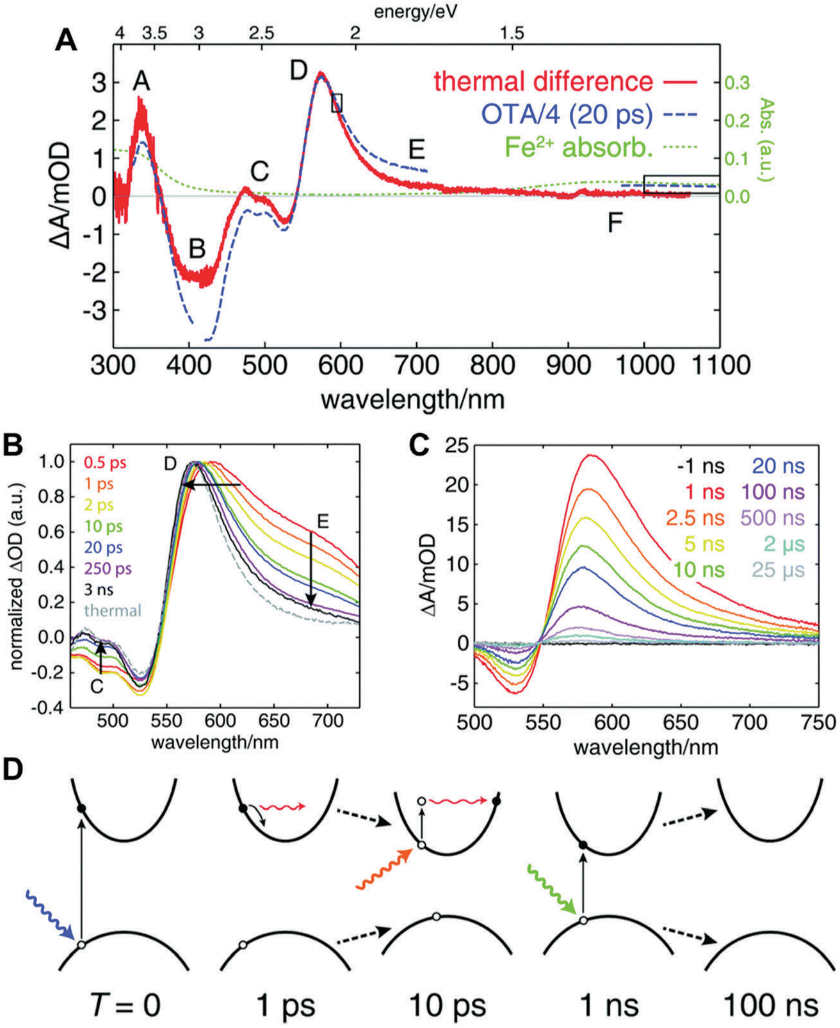

Fig. 10 (A) The thermal difference spectrum (in mOD) of a hematite thin film obtained by subtracting the absorption spectrum obtained at 300 K from the spectrum obtained at 500 K (red solid line) contains all of the same qualitative features as the differential absorption spectrum obtained 20 ps after excitation at λ_{pump} = 415 nm (scaled by a factor of 0.25 for comparison, blue dashed line). The absorption spectrum of $[\mathrm{Fe(H_2O)_6}]^{2+}$ (green dotted line) is shown to account for the NIR absorbance of transient Fe^{2+} species. (B) Normalized differential absorption spectra obtained at various delay times of hematite thin films compared with the normalized thermal difference spectrum (gray dashed line). The labeled regions correspond to those shown in part A. (C) Differential absorption spectra of a hematite film obtained at delay times ranging from 1 ns to 25 μs following excitation at λ_{pump} = 425 nm indicate that lattice cooling persists into the microsecond regime. (D) Schematic illustrating the proposed mechanism and timescale of excited state absorption and lattice thermalization in hematite thin films. Adapted from ref. 4 with permission from The Royal Society of Chemistry.

wavelength throughout the UV and visible regions (λ_{pump} = 277–830 nm) had no significant impact on the shape of the observed transient absorption spectrum. Furthermore, transient X-ray absorption measurements at the oxygen K-edge confirm the bandgap shrinkage observed in the optical transient absorption spectrum.[4] The authors summarized the concurrent thermal and electronic dynamics with the scheme shown in Fig. 10D. Excitation above the bandgap yields a hot carrier in the conduction band that thermalizes to the bottom of the band within one picosecond *via* phonon emission. The bandgap shrinks upon absorption of the thermal energy imparted to the lattice by the phonon emission process, which produces the thermal features in the TA spectrum. Within 10 ps, free carrier absorption gives rise to the additional absorption feature centered at ~675 nm (in region E). Carrier recombination is complete within 100 ps, leaving only red-shifted ground state absorption by one nanosecond after photoexcitation. Finally, lattice cooling to ambient temperature slowly causes the decay of the thermal signals.[4]

Smolin *et al.* recently identified similar thermal effects in a transient absorption study of two perovskite oxide semiconductors: $\mathrm{LaFeO_3}$ and $\mathrm{LaMnO_3}$.[10] By creating a type-I heterojunction $(\mathrm{LaFeO_3})_{52}/(\mathrm{LaMnO_3})_{51}$ bilayer film, the authors were able to identify the purely thermal contributions of the transient absorption spectrum of $\mathrm{LaFeO_3}$. Because $\mathrm{LaMnO_3}$ has a smaller bandgap than $\mathrm{LaFeO_3}$, selective excitation across the bandgap of $\mathrm{LaMnO_3}$ allows only the transfer of heat to $\mathrm{LaFeO_3}$ while excited carriers are confined to $\mathrm{LaMnO_3}$. A schematic of this

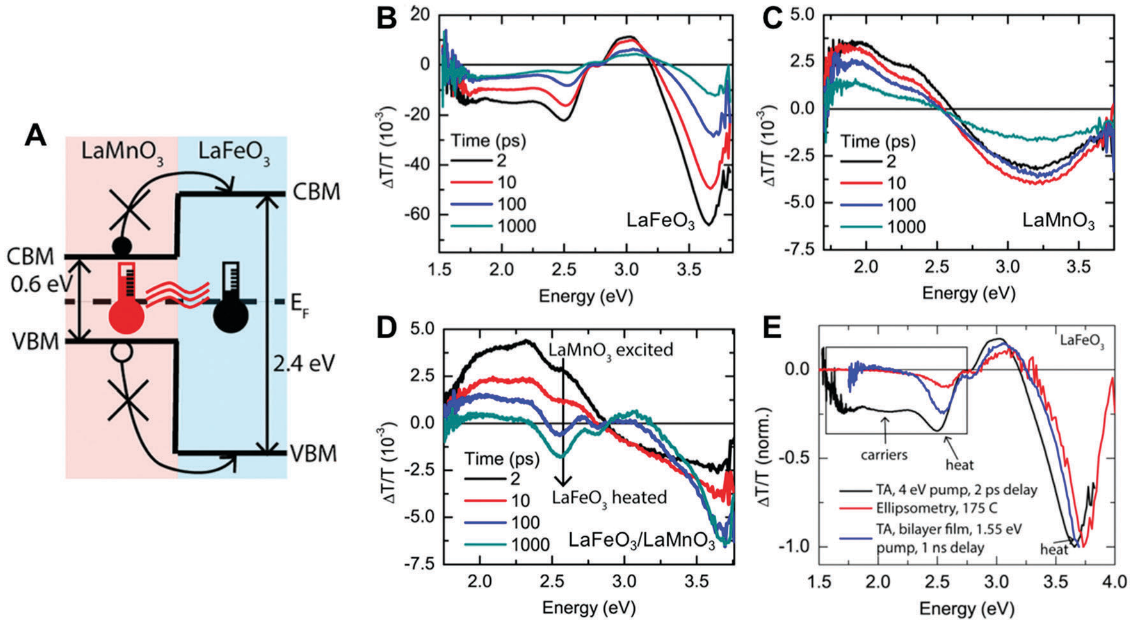

Fig. 11 (A) Schematic of LaFeO$_3$/LaMnO$_3$ heterojunction. (B–D) Representative differential transmission spectra of LaFeO$_3$ (B), LaMnO$_3$ (C), and the type-I LaFeO$_3$/LaMnO$_3$ bilayer heterojunction (D) collected at pump–probe delays of 2, 10, 100, and 1000 ps. (E) Differential transmission spectrum of LaFeO$_3$ collected at a pump–probe delay time of 2 ps (black), thermal difference transmission spectrum of LeFeO$_3$ (red), and the differential transmission spectrum of the bilayer film collected at a pump–probe delay time of 1000 ps (black). Adapted with permission from ref. 10. Copyright 2018 American Chemical Society.

heterojunction is shown in Fig. 11 along with representative transient absorption spectra of LaFeO$_3$, LaMnO$_3$, and the bilayer heterojunction.[64]

As clearly seen in Fig. 11D, the transient absorption spectrum of the selectively excited heterojunction contains many of the same qualitative features as the LaFeO$_3$ transient absorption spectrum after approximately 100 ps. Given the type-I band structure of the heterojunction, the authors conclude that these features are due primarily to transfer of heat to the LaFeO$_3$ lattice. The thermal nature of these spectral features was further confirmed by comparison to the thermal difference spectrum, collected *via* variable angle ellipsometry, shown in Fig. 11E. Discrepancies between the features of the transient absorption spectrum of LaFeO$_3$ and those of the thermal difference spectrum and the transient absorption spectrum of the heterojunction were used to identify spectral regions associated with carrier dynamics.[64]

These recent studies of the dynamics of photoexcited states of organic and metal oxide semiconductor thin films demonstrate the need for great care in interpretation of optical transient absorption data, particularly in the assignment of observed signals to specific transitions. The high peak power of the sub-picosecond laser pulses required for ultrafast pump–probe spectroscopy leads to the indirect transfer of a significant amount of thermal energy to the lattice *via* hot carrier relaxation by phonon scattering. Given the well-established temperature-dependence of bandgap energy,[65] thermal processes of this nature must be considered when interpreting transient absorption spectra of thin-film semiconductor systems in order to distinguish charge-carrier dynamics from transient thermal lattice expansion.[10]

5. Summary and outlook

The recent work highlighted in this review demonstrates the continued utility of ultrafast transient absorption spectroscopy as a method to characterize the dynamics of photogenerated charge carriers in semiconductor thin films, particularly when combined with electrochemical or microscopy techniques. Understanding these dynamics is critical to optimizing the function and performance of solution-processed semiconductor films in optoelectronic devices.

In most device architectures, the photoactive semiconductor film is just one of many functional layers, and device performance relies on transport of photogenerated charge carriers between multiple layers. Transient absorption spectroelectrochemistry provides a useful tool to investigate mechanisms of interlayer charge transport. In particular, the transient absorption spectroelectrochemistry studies highlighted here demonstrate how interfacial depletion regions and trap state densities impact the lifetime of charge-separated states. Such *in operando* measurements are particularly useful for characterizing photoelectrocatalytic systems, although, to date, these measurements have only been reported for n-type photoanode systems. Similar studies of p-type photocathodes will provide information regarding the mechanisms that limit the efficiency of photoelectrochemical reduction of protons or carbon dioxide at these electrodes, which is crucial for the development of purely solar-driven fuel production. Furthermore, the recent demonstration of spectroelectrochemistry in the terahertz regime[66] will enable transient absorption spectroelectrochemistry with a visible pump and terahertz probe. These measurements will be able to distinguish between the transient populations of free and bound carriers under applied electrochemical bias.

Recent transient absorption microscopy studies of semiconductor thin films reveal correlations between spatial heterogeneity of excited state dynamics and the complex morphology of a solution-processed semiconductor film. TAM was also recently demonstrated as an all-optical technique for direct imaging of carrier transport and enabled the recent discovery of a previously unknown localized electronic state in $CH_3NH_3PbI_3$ with a spectral signature obscured in conventional bulk TA measurements. Future improvements in spatial resolution using super-resolution imaging techniques, such as stimulated emission depletion (STED) pumping schemes,[67] will increase the capability of transient absorption microscopy to provide detailed insights into the role of complex morphology on dynamics of photoexcited states in semiconductor thin films.

Finally, recent identification of large thermal contributions to transient absorption spectra of organic and metal oxide semiconductors may be the most unexpected observation made in pump–probe spectroscopy of semiconductor thin films over the last few years. This work calls into question spectral assignments of long-lived photoinduced absorption features in metal oxide semiconductors exclusively to transitions involving free or trapped carriers. On the other hand, the observations of a significant dependence of the dynamics of these features on the magnitude of an applied bias is consistent with assignment of some contribution of free carriers to these signals. More experiments are required to reconcile these seemingly disparate observations.

In summary, the work reviewed here highlights three recent innovations in ultrafast transient absorption spectroscopy applied to solution-processed semiconductor thin films. Continuing improvements in the capability, stability, and availability of ultrafast laser systems, and their decreasing cost, combined with rapid and continuous advances in development of new materials and film fabrication techniques promise future innovations in, and the ongoing relevance of, ultrafast transient absorption spectroscopy of semiconductor thin films.

Conflicts of interest

There are no conflicts to declare.

Acknowledgements

The authors gratefully acknowledge the financial support of start-up funds from the University of Rochester.

References

1 L. X. Chen, in *X-Ray Absorption and X-Ray Emission Spectroscopy: Theory and Applications*, ed. J. A. Van Bokhoven and C. Lamberti, John Wiley & Sons, Ltd, Chichester, UK, 2016, ch. 9, pp. 213–249.

2 Z.-H. Loh and S. R. Leone, *J. Phys. Chem. Lett.*, 2013, **4**, 292–302.

3 M.-F. Lin, M. A. Verkamp, J. Leveillee, E. S. Ryland, K. Benke, K. Zhang, C. Weninger, X. Shen, R. Li, D. Fritz, U. Bergmann, X. Wang, A. Schleife and J. Vura-Weis, *J. Phys. Chem. C*, 2017, **121**, 27886–27893.

4 D. Hayes, R. G. Hadt, J. D. Emery, A. A. Cordones, A. B. F. Martinson, M. L. Shelby, K. A. Fransted, P. D. Dahlberg, J. Hong, X. Zhang, Q. Kong, R. W. Schoenlein and L. X. Chen, *Energy Environ. Sci.*, 2016, **9**, 3754–3769.

5 S. Biswas, J. Husek, S. Londo and L. R. Baker, *Nano Lett.*, 2018, **18**, 1228–1233.

6 J. B. Baxter and G. W. Guglietta, *Anal. Chem.*, 2011, **83**, 4342–4368.

7 J. Peng, Y. Chen, K. Zheng, T. Pullerits and Z. Liang, *Chem. Soc. Rev.*, 2017, **46**, 5714–5729.

8 E. O. Göbel, *Opt. Photonics News*, 1992, **3**, 33–39.

9 J. Shah, *Ultrafast Spectroscopy of Semiconductors and Semiconductor Nanostructures*, Springer, New York, 1996.

10 S. Y. Smolin, A. K. Choquette, J. Wang, S. J. May and J. B. Baxter, *J. Phys. Chem. C*, 2018, **122**, 115–123.

11 P. Würfel and U. Würfel, *Physics of Solar Cells: From Basic Principles to Advanced Concepts*, Wiley-VCH, Weinheim, Germany, 3rd edn, 2016.

12 A. J. Bard, *J. Photochem.*, 1979, **10**, 59–75.

13 M. G. Walter, E. L. Warren, J. R. McKone, S. W. Boettcher, Q. Mi, E. A. Santori and N. S. Lewis, *Chem. Rev.*, 2010, **110**, 6446–6473.

14 L. M. Peter, in *Photocatalysis: Fundamentals and Perspectives*, ed. J. Schneider, D. Bahnemann, J. Ye, G. L. Puma and D. D. Dionysiou, The Royal Society of Chemistry, Cambridge, UK, 2016, ch. 1, pp. 1–28.

15 Z. Huang, Y. Lin, X. Xiang, W. Rodriguez-Córdoba, K. J. McDonald, K. S. Hagen, K.-S. Choi, B. S. Brunschwig, D. G. Musaev, C. L. Hill, D. Wang and T. Lian, *Energy Environ. Sci.*, 2012, **5**, 8923–8926.

16 S. R. Pendlebury, A. J. Cowan, M. Barroso, K. Sivula, J. Ye, M. Grätzel, D. R. Klug, J. Tang and J. R. Durrant, *Energy Environ. Sci.*, 2012, **5**, 6304–6312.

17 F. Le Formal, S. R. Pendlebury, M. Cornuz, S. D. Tilley, M. Grätzel and J. R. Durrant, *J. Am. Chem. Soc.*, 2014, **136**, 2564–2574.

18 S. R. Pendlebury, X. Wang, F. Le Formal, M. Cornuz, A. Kafizas, S. D. Tilley, M. Grätzel and J. R. Durrant, *J. Am. Chem. Soc.*, 2014, **136**, 9854–9857.

19 A. J. Cowan, J. Tang, W. Leng, J. R. Durrant and D. R. Klug, *J. Phys. Chem. C*, 2010, **114**, 4208–4214.

20 Y. Ma, S. R. Pendlebury, A. Reynal, F. Le Formal and J. R. Durrant, *Chem. Sci.*, 2014, **5**, 2964–2973.

21 J. Ravensbergen, F. F. Abdi, J. H. van Santen, R. N. Frese, B. Dam, R. van de Krol and J. T. M. Kennis, *J. Phys. Chem. C*, 2014, **118**, 27793–27800.

22 M. Barroso, S. R. Pendlebury, A. J. Cowan and J. R. Durrant, *Chem. Sci.*, 2013, **4**, 2724–2734.

23 R. Godin, A. Kafizas and J. R. Durrant, *Curr. Opin. Electrochem.*, 2017, **2**, 136–143.

24 M. A. Green, A. Ho-Baillie and H. J. Snaith, *Nat. Photonics*, 2014, **8**, 506–514.

25 G. F. Samu, R. A. Scheidt, P. V. Kamat and C. Janáky, *Chem. Mater.*, 2018, **30**, 561–569.

26 R. A. Scheidt, G. F. Samu, C. Janáky and P. V. Kamat, *J. Am. Chem. Soc.*, 2018, **140**, 86–89.

27 F. Odobel and Y. Pellegrin, *J. Phys. Chem. Lett.*, 2013, **4**, 2551–2564.

28 F. Odobel, L. Le Pleux, Y. Pellegrin and E. Blart, *Acc. Chem. Res.*, 2010, **43**, 1063–1071.

29 R. J. Dillon, L. Alibabaei, T. J. Meyer and J. M. Papanikolas, *ACS Appl. Mater. Interfaces*, 2017, **9**, 26786–26796.

30 E. M. Grumstrup, M. M. Gabriel, E. E. M. Cating, E. M. Van Goethem and J. M. Papanikolas, *Chem. Phys.*, 2015, **458**, 30–40.

31 Z. Guo, J. S. Manser, Y. Wan, P. V. Kamat and L. Huang, *Nat. Commun.*, 2015, **6**, 7471.

32 T. Virgili, G. Grancini, E. Molotokaite, I. Suarez-Lopez, S. K. Rajendran, A. Liscio, V. Palermo, G. Lanzani, D. Polli and G. Cerullo, *Nanoscale*, 2012, **4**, 2219–2226.

33 L. Huang and J.-X. Cheng, *Annu. Rev. Mater. Res.*, 2013, **43**, 213–236.

34 M. C. Fischer, J. W. Wilson, F. E. Robles and W. S. Warren, *Rev. Sci. Instrum.*, 2016, **87**, 031101.

35 G. V. Hartland, *Chem. Sci.*, 2010, **1**, 303–309.

36 D. Polli, G. Grancini, J. Clark, M. Celebrano, T. Virgili, G. Cerullo and G. Lanzani, *Adv. Mater.*, 2010, **22**, 3048–3051.

37 C. T. O. Wong, S. S. Lo and L. Huang, *J. Phys. Chem. Lett.*, 2012, **3**, 879–884.

38 G. Grancini, D. Polli, D. Fazzi, J. Cabanillas-Gonzalez, G. Cerullo and G. Lanzani, *J. Phys. Chem. Lett.*, 2011, **2**, 1099–1105.

39 C. Y. Wong, S. B. Penwell, B. L. Cotts, R. Noriega, H. Wu and N. S. Ginsberg, *J. Phys. Chem. C*, 2013, **117**, 22111–22122.

40 T. Katayama, A. Jinno, E. Takeuchi, S. Ito, M. Endo, A. Wakamiya, Y. Murata, Y. Ogomi, S. Hayase and H. Miyasaka, *Chem. Lett.*, 2014, **43**, 1656–1658.

41 M. J. Simpson, B. Doughty, B. Yang, K. Xiao and Y.-Z. Ma, *J. Phys. Chem. Lett.*, 2015, **6**, 3041–3047.

42 B. Doughty, M. J. Simpson, B. Yang, K. Xiao and Y.-Z. Ma, *Nanotechnology*, 2016, **27**, 114002.

43 M. J. Simpson, B. Doughty, B. Yang, K. Xiao and Y.-Z. Ma, *J. Phys. Chem. Lett.*, 2016, **7**, 1725–1731.

44 S. Nah, B. Spokoyny, C. Stoumpos, C. M. M. Soe, M. Kanatzidis and E. Harel, *Nat. Photonics*, 2017, **11**, 285–288.

45 M. J. Simpson, B. Doughty, S. Das, K. Xiao and Y.-Z. Ma, *J. Phys. Chem. Lett.*, 2017, **8**, 3299–3305.

46 Z. Guo, Y. Wan, M. Yang, J. Snaider, K. Zhu and L. Huang, *Science*, 2017, **356**, 59–62.

47 Q. A. Alsulami, B. Murali, Y. Alsinan, M. R. Parida, S. M. Aly and O. F. Mohammed, *Adv. Energy Mater.*, 2016, **6**, 1502356.

48 S. Günes, H. Neugebauer and N. S. Sariciftci, *Chem. Rev.*, 2007, **107**, 1324–1338.

49 M. C. Scharber and N. S. Sariciftci, *Prog. Polym. Sci.*, 2013, **38**, 1929–1940.

50 M. Campoy-Quiles, T. Ferenczi, T. Agostinelli, P. G. Etchegoin, Y. Kim, T. D. Anthopoulos, P. N. Stavrinou, D. D. C. Bradley and J. Nelson, *Nat. Mater.*, 2008, **7**, 158–164.

51 B. Kippelen and J.-L. Brédas, *Energy Environ. Sci.*, 2009, **2**, 251–261.

52 M. B. Smith and J. Michl, *Chem. Rev.*, 2010, **110**, 6891–6936.

53 Y. Wan, Z. Guo, T. Zhu, S. Yan, J. Johnson and L. Huang, *Nat. Chem.*, 2015, **7**, 785–792.

54 G. B. Piland and C. J. Bardeen, *J. Phys. Chem. Lett.*, 2015, **6**, 1841–1846.

55 L. M. Herz, *Annu. Rev. Phys. Chem.*, 2016, **67**, 65–89.

56 J. S. Manser, J. A. Christians and P. V. Kamat, *Chem. Rev.*, 2016, **116**, 12956–13008.

57 S. Nah, B. Spokoyny, X. Jiang, C. Stoumpos, C. M. M. Soe, M. G. Kanatzidis and E. Harel, *Nano Lett.*, 2018, **18**, 827–831.

58 S. Albert-Seifried and R. H. Friend, *Appl. Phys. Lett.*, 2011, **98**, 223304.

59 A. Rao, M. W. B. Wilson, S. Albert-Seifried, R. Di Pietro and R. H. Friend, *Phys. Rev. B*, 2011, **84**, 195411.

60 A. K. Le, J. A. Bender and S. T. Roberts, *J. Phys. Chem. Lett.*, 2016, **7**, 4922–4928.

61 N. J. Cherepy, D. B. Liston, J. A. Lovejoy, H. Deng and J. Z. Zhang, *J. Phys. Chem. B*, 1998, **102**, 770–776.

62 A. G. Joly, J. R. Williams, S. A. Chambers, G. Xiong, W. P. Hess and D. M. Laman, *J. Appl. Phys.*, 2006, **99**, 053521.

63 S. Sorenson, E. Driscoll, S. Haghighat and J. M. Dawlaty, *J. Phys. Chem. C*, 2014, **118**, 23621–23626.

64 S. Y. Smolin, A. K. Choquette, J. Wang, S. J. May and J. B. Baxter, *J. Phys. Chem. C*, 2018, **122**, 115–123.

65 Y. P. Varshni, *Physica*, 1967, **34**, 149–154.

66 C. T. Nemes, J. R. Swierk and C. A. Schmuttenmaer, *Anal. Chem.*, 2018, **90**, 4389–4396.

67 S. B. Penwell, L. D. S. Ginsberg, R. Noriega and N. S. Ginsberg, *Nat. Mater.*, 2017, **16**, 1136–1141.